Materials & Design 233 (2023) 112216

Contents lists available at ScienceDirect

Materials & Design

journal homepage: www.elsevier.com/locate/matdes

4D printing of recoverable buckling-induced architected iron-based shape memory alloys

A. Jafarabadi [a,b,e], I. Ferretto [a], M. Mohri [a], C. Leinenbach [a,c], E. Ghafoori [a,b,d,*]

[a] Empa, Swiss Federal Laboratories for Materials Science and Technology, Dübendorf 8600, Switzerland
[b] Institute of Structural Engineering, Swiss Federal Institute of Technology Zürich (ETH-Zürich), 8093 Zürich, Switzerland
[c] Laboratory for Photonic Materials and Characterization, École Polytechnique Fédérale de Lausanne (EPFL), 1015 Lausanne, Switzerland
[d] Institute for Steel Construction, Faculty of Civil Engineering and Geodetic Science, Leibniz University Hannover, 30167 Hannover, Germany
[e] School of Civil Engineering, University of Tehran, 16th Azar Street, Tehran, Iran

ARTICLE INFO

Keywords:
Architected materials
Fe-based shape memory alloys
Energy absorption
Shape recovery
Energy dissipation
Snap-through
Laser powder bed fusion
3D and 4D metal printing

ABSTRACT

Architected materials exhibit extraordinary properties in comparison with conventional materials and structures, resulting in additional functionality and efficiency by engineering the geometry in harmony with the base material. Buckling-induced architected materials (BIAMs) are a class of architected materials that exhibit a significant potential to absorb and dissipate energy owing to their local instabilities. Previous studies have shown a trade-off between energy dissipation and geometrical recoverability in metallic BIAM, which limits their use in applications that require both of these features. This study, for the first time, presents 4D printing of buckling-induced architected iron-based shape memory alloys (BIA Fe-SMAs) using laser powder bed fusion (LPBF). The results show that 4D printing of BIA Fe-SMAs can offer both energy dissipation and geometrical recoverability (i.e., recentring). The study was conducted on two different alloy compositions of Fe-17Mn-5Si-10Cr-4Ni. Quasi-static cyclic tests were performed on the two BIA Fe-SMAs, and the samples were subsequently heated to 200 °C to activate the shape memory effect (SME) of the base material. The samples could recover the residual deformations accumulated during the cyclic load owing to the SME of the base material, which led to shape-recovery ratios of 96.8 and 98.7% for the studied BIA Fe-SMAs. The results of this study demonstrate that 4D printing of BIA Fe-SMAs can yield an enhanced multi-functional behavior by combining the material's inherent functional behavior with the functionalities of the architected structure. Notably, BIA Fe-SMA samples could reconfigure their initial shape without damage after densification, which sets them apart from conventional crushable lattices.

1. Introduction

Additive manufacturing technologies have enabled engineers to design structures to not only increase material efficiency but also introduce a multifunctionality [1,2]. Metal additive manufacturing facilitates the proof of new engineering design concepts owing to its fast and cheap prototyping [3]. Combining architected metastructures and smart materials has significant potential for shaping the future of engineered structures. Therefore, by integrating cellular architected patterns into the design of structural components, extraordinary properties can be manifested compared with conventional materials and structures, which include negative stiffness [4–11] and negative Poisson's ratio [12–14] and damage-tolerant densification [15] with significant energy absorption. Development of such architected materials, considering their multi-functionality and weight saving may accelerate the realization of sustainable development objectives. Moreover, recent studies have proven the possibility of utilizing metal additive manufacturing in scale through practical examples [16–19].

Buckling-induced architected materials (BIAMs) have been widely studied because of their significant impact and shock absorption capacity [2,5,7,8,20–26]. In this study, buckling induced architected Fe-based shape memory alloys (BIA Fe-SMA) are introduced as particular type of BIAMs. A schematic view of the BIA Fe-SMA assembly that is utilized in this study is shown in Fig. 1a. Further details regarding the configuration and design are discussed in the Design Considerations section. BIAMs can be tuned for bi-stable or mono-stable responses [27,28], as shown in Fig. 1b. In a mono-stable design, the curved beams snap-back after exhibiting a snap-through instability, indicating that the initial shape recovers upon unloading. However, in a bi-stable design,

* Corresponding author at: Empa, Swiss Federal Laboratories for Materials Science and Technology, Dübendorf 8600, Switzerland.
E-mail address: ghafoori@stahl.uni-hannover.de (E. Ghafoori).

https://doi.org/10.1016/j.matdes.2023.112216
Received 23 March 2023; Received in revised form 22 May 2023; Accepted 31 July 2023
Available online 7 August 2023

Nomenclature

δ	Displacement
BIAM	Buckling-induced architected materials
$\delta_{cycle-1}$	Major residual deformation after first loading cycle
BIA Fe − SMA	Buckling-induced architected Fe-based shape memory alloy
$\delta_{activation}$	Deformation recovery due to activation
SME	Shape memory effect
$\omega(x)$	Height of the curved beam
PE	Pseudoelasticity
h	Apex height of the curved beam
VC +	Composition Fe-17Mn-5Si-10Cr-4Ni-1 (V,C)
l	Length of the curved beam
nVC	Composition Fe-17Mn-5Si-10Cr-4Ni-1
Q = h/t	Stability state ratio
FEA	Finite element analysis
ts	Thickness of side columns
L − *PBF*	Laser powder bed fusion
tb	Thickness of bottom beam
EDM	Electrical discharge machining
F	Reaction force
V	Volume
R_r	Recovery ratio
SEA	Specific energy absorption
R_{ra}	Accumulated shape-recovery ratios
SED	Specific energy dissipation
δ_r	Recovered displacement after unloading
W_d	Dissipated energy
δ_m	Maximum induced compressive deformation
ε_n	Nominal strain
$\sigma_{0.2\%}$	Proof stress
W_a	Absorbed energy
A_s	Austenitic start temperature
H	Initial height of the samples
A_s	Austenitic finish temperature

the BIAM remains in the second stable configuration after loading without self-recovering its original stable state (Fig. 1b).

Although both bi-stable and mono-stable BIAMs have been thoroughly studied in the literature [2,6,8,10,20,21,29–33], there are only a limited studies on metallic BIAMs [7,34,35]. In contrast to polymer-based BIAMs, metallic lattices exhibit a relatively high force threshold (instability force) because of their significantly higher elastic moduli. However, because of the glass transition temperature limitation in polymers, the serviceability temperature is typically lower than that of metallic lattices. The metallic BIAMs, as illustrated in Fig. 1c and 1d, can be designed for an elastic [7] or inelastic [35] response, which comes at the expense of negligible energy dissipation and reversibility, respectively. It should be noted that in polymeric BIAMs, both recoverability and energy dissipation occur simultaneously, owing to the inherent

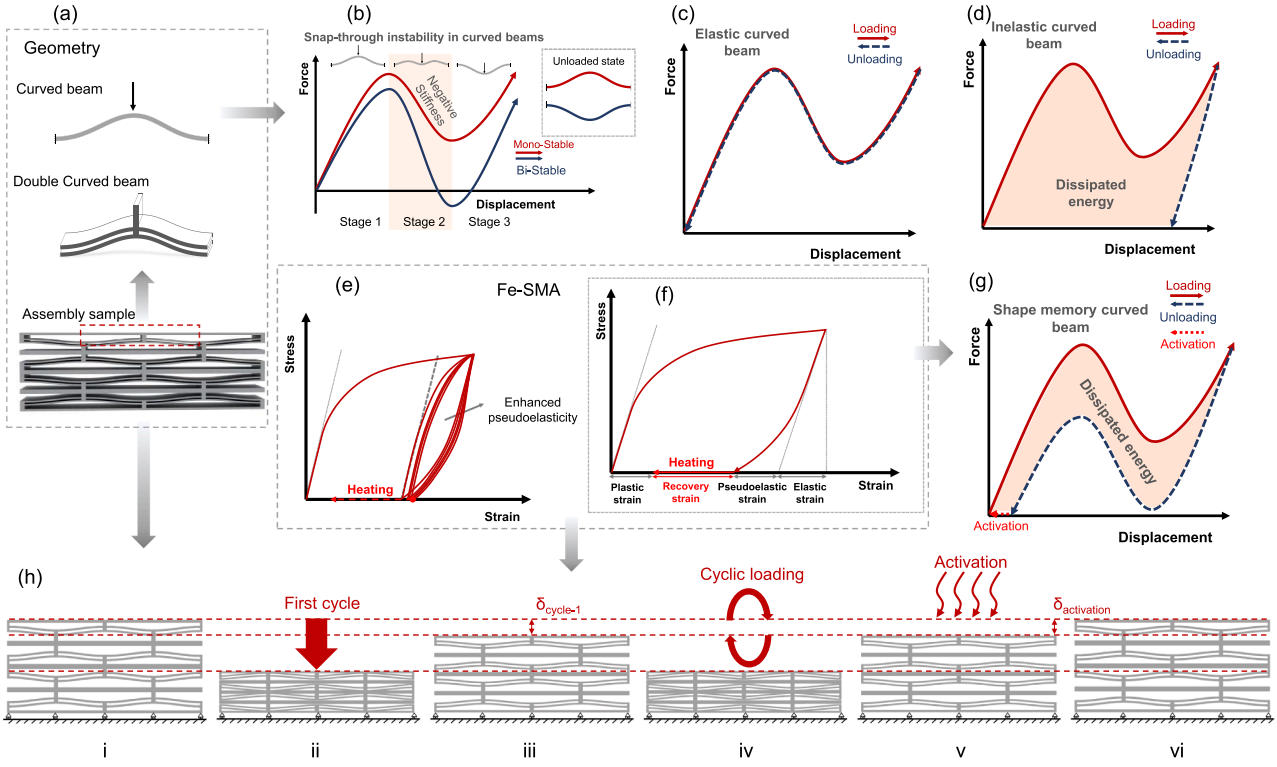

Fig. 1. Schematic view of energy dissipation mechanism in BIA Fe-SMAs. a) Architecture of the BIA Fe-SMA samples consists of double curved beam elements, which govern the response of the structure. b) Schematic of the mono-stable and bi-stable responses in a laterally loaded curved beam. While in the absence of the external load, the mono-stable mechanism recovers the initial stable state; both mechanisms similarly exhibit a negative stiffness region in the force–displacement response, which is due to the snap-through instability. c) Response of a metallic mono-stable elastic curved beam that exhibits shape-recovery and negligible energy dissipation. d) Response of a metallic mono-stable inelastic curved beam that exhibits energy dissipation however, it is followed by significant permanent displacement. e) Force-controlled cyclic behavior of the Fe-SMA. f) Tensile load-unload behavior of the Fe-SMA. g) Response of a Fe-SMA mono-stable inelastic curved beam in which shape-recovery and energy dissipation occur concurrently owing to PE and SME in the based material. h) BIA Fe-SMA sample under cyclic compression tests. $\delta_{cycle-1}$ is the major residual deformation that occurs after the first cycle and is almost counterbalanced by $\delta_{activation}$ owing to activation of SME.

damping property of the base material.

To overcome this inevitable trade-off in metallic BIAMs, a novel design using Fe-based shape memory alloys (Fe-SMAs) was introduced in this study. Two compositions of Fe-17Mn-5Si-10Cr-4Ni-1(V,C) and Fe-17Mn-5Si-10Cr-4Ni (without V and C), hereafter VC + and nVC, respectively, were used for the fabrication of the samples. Buckling-induced architected Fe-SMAs (BIA Fe-SMAs) have the advantage of a base material with an inherent damping capacity in addition to a high elastic modulus. The damping capacity of SMAs is derived from the pseudo-elastic behavior of this class of alloys. This is because of the energy required for phase transformations to occur. The movement of austenite–martensite interfaces and interfaces between martensite variants generates high internal friction, which contributes to the damping effect. Thus, Fe-SMAs are suitable candidates for applications such as dampers and impact mitigators in large engineering structures owing to their good shape memory effect (SME), low production cost, good workability and ductility [36], large stress–strain hysteresis, high elastic modulus, and pseudo-elasticity (PE) [37,38].

A schematic of the cyclic loading–unloading behavior (under a constant stress level) of an Fe-SMA is shown in Fig. 1e. During loading, the nonlinear deformation behavior after elastic deformation was due to martensitic transformation, followed by both plastic and martensitic transformations. There was a considerable residual strain in the first step. However, the residual strain was significantly reduced in the subsequent cycles. The reverse transformation (martensite to austenite) resulting in the improvement of the PE and increased work-hardening under cyclic loading was studied in [39,40]. Fig. 1f schematically illustrates the material behavior of the Fe-SMAs at room temperature. The PE effect occurs as a result of a stress-induced martensitic transformation from an austenite (γ-FCC) phase to a martensite (ε-HCP) phase during loading, and its inverse phase transformation (ε to γ) during unloading. Subsequently, by heating the material above the austenite start temperature (activation), the SME occurs as a consequence of a reverse phase transformation (ε to γ), leading to the recovery of a significant amount of induced residual deformation [36,41]. Therefore, the same phenomena occur in Fe-SMA curved beam elements (Fig. 1a), where the mono-stability, as well as the PE effect, enhances the reversibility of the beam, which leads to minimal residual deformations upon unloading (Fig. 1g). Moreover, owing to the SME, if properly designed to avoid large plastic deformations, the residual deformation can be recovered by heating the lattices.

A summary of the BIA SMAs studied in the present study is schematically shown in Fig. 1h. Responses were classified into six stages. The initial stage of the BIA Fe-SMA is shown in Fig. 1h.i. in the second stage, the sample is loaded up to the deification and unloaded subsequently (Fig. 1h.ii). Consequently, after the first loading cycle, a major residual deformation, $\delta_{cycle\text{-}1}$, is induced (Fig. 1h.iii). Then, a series of cyclic loading and unloading cycles was applied, which resulted in almost full recoverability and negligible residual deformation compared to the first cycle (Fig. 1h.iv). This is justified by the fact that owing to residual deformation, which is primarily related to the first cycle, the strain demand for the curved beam decreases. In contrast, the base material exhibited an enhanced PE for the following cycles after the first cycle. Eventually, the BIA Fe-SMA samples were heated in a controlled furnace (Fig. 1h.v) which led to almost a full shape recovery (Fig. 1h.vi). The details of each stage are discussed in the following sections.

2. Materials and methods

2.1. Design and additive manufacturing of buckling-induced architected Fe-SMA

The BIA Fe-SMA has a 2.5D configuration, implying that the 2D plane is uniformly extruded along the third direction. The main motivation for choosing mono-stable curved beams for the cell configuration is the concurrent presence of shape-recovery and energy absorption. While crushable architected materials exhibit more promising energy absorption in comparison to mono-stable curved beams, the shape recovery performance remains poor due to extensive damage. Mono-stable curved beams demonstrate snap-through instability when subjected to lateral loading. When the external load is removed, the curved beams snap back to their original configuration. Therefore, it can undergo substantial deformations and return to its original configuration without experiencing significant damage.

The configuration consists of straight and cosine-curved elements. The curved elements were stacked in a double configuration and laterally loaded by straight columns when compressed (Fig. 2). Using a double curved beam configuration suppresses the tendency of the curved beam for out-of-plane lateral buckling as well as asymmetric in-plane buckling, which affects the snap-through behavior [28]. The curved beams are clamped to a straight column at each end. The columns were thicker than the beams, which provided a fixed boundary condition. In this manner, the beams suddenly release the stored strain energy, resulting in the snap-through of the beams. Furthermore, in a mono-stable configuration, the straight beams contribute to the shape recovery of the BIAM by facilitating snap-back of the curved beams. The cosine-curved beam profile has the same shape as the first buckling mode of an axially loaded column (Fig. 2), which is expressed as [28] $\omega(x) = h/2\left[1 - cos\left(\frac{2\pi x}{l}\right)\right]$. The geometrical parameters defining the curved beam's shape include the height of the curved beam from the horizon at the length × (ω), the apex height of the curved beam (h), the length of the curved beam (l), the in-plane thickness of the curved beam (t), and the out-of-plane thickness (b), as shown in Fig. 2a and Table 1.

The stability state of curved beams can be characterized by Q, which is the ratio of h/t. Theoretically, if $Q < 2.31$, the curved beam exhibits a mono-stable response, implying that the beam has only one stable state [28]. That is, upon unloading, the curved beam retained its stable configuration. Furthermore, $Q \geq 2.31$ will result in a bi-stable configuration, implying that in the absence of an external load, the curved beam will remain in the second stable state after the snap-through. However, these values were based on a perfectly elastic material with a rigid boundary condition [42]. In practice, particularly in BIA Fe-SMAs, none of the assumptions are valid; therefore, curved beams are monostable for greater values of Q [7]. The stability state of the beam was examined using finite element analysis (FEA), and for a Q of 2.4, the BIA Fe-SMA exhibited a mono-stable response. Another design constraint is the level of induced strain in the curved beams. In other words, by adjusting the geometry, the amount of the induced strain in the base material can be engineered [43]. The induced strain affects the response of the samples in terms of energy absorption, energy dissipation and recoverability. Thus, based on material-level studies on additively manufactured Fe-SMAs [39,44,45], BIAMs are designed to limit the maximum induced strain to approximately 1%, leading to a proper trade-off between the energy dissipation and recoverability of the BIA Fe-SMAs. To initially adjust the geometrical parameters, the estimation of the maximum strain (ε_{max}) in the curved beams during snap-through [28] was calculated as follows:

$$\varepsilon_{max} \approx \pi^2 \frac{th}{l^2}\left(2 + \frac{4}{3Q}\right) = \pi^2 \frac{0.5 \times 1.2}{38^2}\left(2 + \frac{4}{3 \times 2.4}\right) = 0.010 \quad (1)$$

Moreover, the distance between curved beams and horizontal beams are adjusted in a way that after snap-through, the curved beams come in contact with the horizontal beams, preventing excessive deformation on the curved beam during densification. In addition to the stability state and induced strain, the build plate of the printing device was another design constraint. Therefore, BIA Fe-SMA samples were designed such that they can be encompassed by the build plate, which has a diameter of 100 mm, for the Sisma MySint 100 laser powder bed fusion (L-PBF) device.

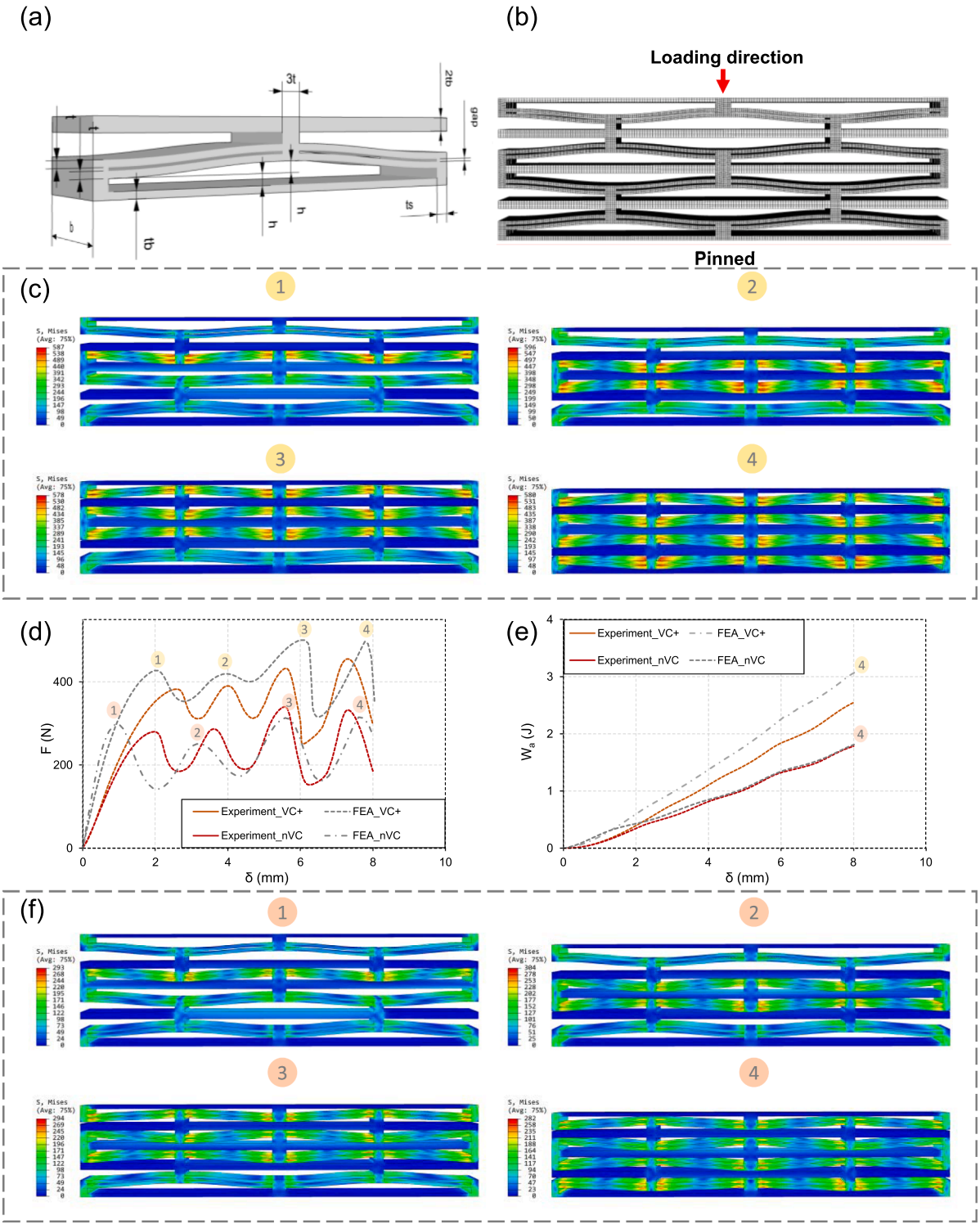

Fig. 2. Parametric CAD generation and FE simulation of the nVC and VC + samples. a) Tunable geometrical parameters of a BIA Fe-SMA unit-cell. b) Grasshopper 3D Graphical algorithm generating the parametric BIAM. c) FE simulation of the VC + sample under compression loading demonstrating the four (1–4) successive snap-through of the curved beams. At the intersection of the curved beams and the vertical elements (joints) stress concentration (Stress values in MPa) occurs. d) Comparison of the compressive loading response of both VC + and nVC samples with the FEA results. e) Comparison of the energy absorption through the compressive loading of the VC + and nVC samples with the experimental results. f) FE simulation of the nVC sample under compression loading demonstrating the four (1–4) successive snap-through of the curved beams.

2.1.1. Parametric design and finite element analysis

To generate such complex architecture in a hierarchical and parametric manner, the geometry of the sample was defined in Grasshopper 3D, which is a visual programming language that runs within the Rhinoceros 3D computer-aided design (CAD) application. The Grasshopper code was primarily developed to generate a versatile parametric unit cell (see Fig. 2a). The final assembly was generated by replicating the unit cell horizontally and vertically. To design and assess the

Table 1
Geometrical properties of the BIA Fe-SMA designed and as-built samples.

	h	t	l	b	tp	ts	gap	n	Q
CAD	1.2	0.5	38	10	1.5	0.75	0.5	2	2.4
As-built	1.1	0.7	38	9.7	1.7	0.9	0.3	2	1.57

stability state of the BIA Fe-SMA samples, a nonlinear finite element analysis was performed using the commercial finite element (FE) package Abaqus CAE 6.23. CAD models, which were generated in the Rhino Grasshopper software, were imported into Abaqus and meshed using C3D8 linear elements (see Fig. 2b). Mesh sensitivity analysis was carried out through different mesh sizes and for linear and quadratic elements in order to ensure computational accuracy. A mesh size of 0.5 mm was adopted for straight beams while for the curved beams, where large deformations occur, a mesh size of 0.25 mm was adopted. A static solver with considerations for geometrical nonlinearity was employed. Pinned boundary condition introduced at the bottom of the sample. In addition, the top surface of the sample was fully coupled with a reference point and a displacement-controlled loading introduced at the reference point in order to compress the samples.

An elasto-plastic material behavior was introduced to the model to evaluate the energy absorption at the maximum loading state. The observed nonlinear stress–strain behavior in Fe-Mn-Si alloys can be attributed to the occurrence of martensite transformation, plastic flow, or a concurrent combination of both phenomena. According to Lee et al. [46], the 0.1% proof stress is more suitable for determining the onset of inelastic stress associated with martensite transformation compared to the 0.2% proof stress. In this study, both the 0.1% and 0.2% proof stresses were calculated and denoted as $\sigma_{0.1\%}$ and $\sigma_{0.2\%}$, respectively, as shown in Fig. 4c. Therefore, for the introduced material behavior in the FEA, inelastic stress–strain behavior starts from $\sigma_{0.1\%}$. Moreover, the elastic modulus derived from the experiments shown in Fig. 4. Ultimately, the true stress–strain behavior was calculated based on the engineering stress–strain values of both alloys and then introduced to the FEA. As the PE property is not introduced to the material model, the simulations are only valid for estimation of compressive strength (i.e., force threshold) and the absorbed energy.

The von Mises stress field for each snap-through sequence (1–4) is illustrated in Fig. 2c and 2f. The results of FEA and experiments on both samples for the first compressive loading stage are illustrated in Fig. 2d. Each labeled apex in Fig. 2d corresponds to a snap-through sequence in Fig. 2c and 2f. The FEA results in terms of energy absorption were compared with the energy absorption obtained from the experimental results (see Fig. 2e). The comparison indicates that the experimental and numerical results for the nVC sample generally agree in predicting the force threshold (compressive strength) and energy absorption. However, for the VC + sample, the force threshold was slightly overestimated, which resulted in a higher energy absorption.

2.1.2. Additive manufacturing process and characterization

The materials chosen for the present study are two batches of the Fe-based SMA Fe-17Mn-5Si-10Cr-4Ni, which has been investigated in our previous studies [44,47]. The Fe-SMA powders were fabricated by gas atomization in an Ar atmosphere from conventional alloys to obtain spherical particles. The VC + powder with a d50 of 33 μm was provided by voestalpine BÖHLER Edelstahl GmbH & Co KG, Kapfenberg, Austria. The nVC powder was produced by Metal Player Co., Ltd., Republic of Korea and had an average size of 30 μm. The composition of the powders is given in Table 2. The main difference between the two powders is the addition of V and C to the VC + powder. According to previous investigations, samples fabricated from VC + powder exhibit more pronounced pseudo-elastic behavior after heat treatment because of the precipitation of (V) and (V and Cr) carbides [45].

A Sisma MySint 100 L-PBF machine (Sisma S.p.A., Italy) was used to fabricate samples. The machine is equipped with a 1070 nm fiber laser with a Gaussian intensity distribution, a spot size of 55 μm, and a maximum output power of 200 W. The oxygen content in the chamber was kept below 0.1% during fabrication. The selected build parameters are summarized in Table 3. The laser power was set to 175 W, the layer thickness to 0.1 mm and the hatch spacing to 0.03 mm. The applied scanning speed was 300 mm/s for the nVC sample, and 225 mm/s for the VC + sample. With these parameters, the greatest density of the LPBF-fabricated parts was achieved.

Table 3 summarizes the selected parameters. The processing parameters were selected in accordance with previous research on the two alloys [44,45], where parametric studies were conducted to identify the optimum laser parameters for dense part fabrication. A bidirectional scanning strategy with a rotation of 90° between the layers was applied to both samples. A slightly lower laser scan velocity was selected for the VC + alloy.

Microstructural characterization was performed using scanning electron microscopy (SEM; FEI NanoSEM230). Samples for SEM observation were polished and etched with a solution of H2O2 (35%), HNO3 (65%), and HCl (32%) at a ratio of 7/30/9.

In addition, two blocks with the dimensions xyz were also printed for both compositions in order study the SME of the printed samples. Dog-bone-shaped tensile specimens with a loading direction perpendicular to the build direction were fabricated from the blocks using electrical discharge machining (EDM). The geometry and dimensions for the dog-bone-shaped specimen is reported in Fig. 4a.

Heat treatments were conducted after fabrication. The nVC alloy was annealed at 800 °C for 2 h based on the previous studies of the authors [44,47] because annealing process relaxes the residual stress developed during the process and dissolves any ferrite formed during the process. The VC + sample was aged directly after manufacturing to induce carbide precipitation. Aging was performed according to the outcome of a previous study of the authors [39,45,48], where the effect of aging conditions on precipitate size and density, and therefore on material

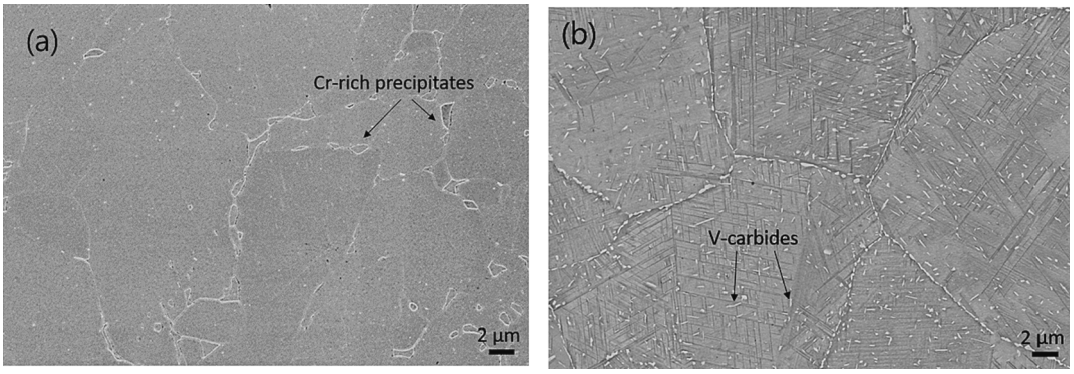

Fig. 3. SEM images of the printed nVC and VC + Fe-SMAs, a) nVC after annealed at 800 °C for 2 h and, b) VC + after heat treatment at 750 °C for 6 h.

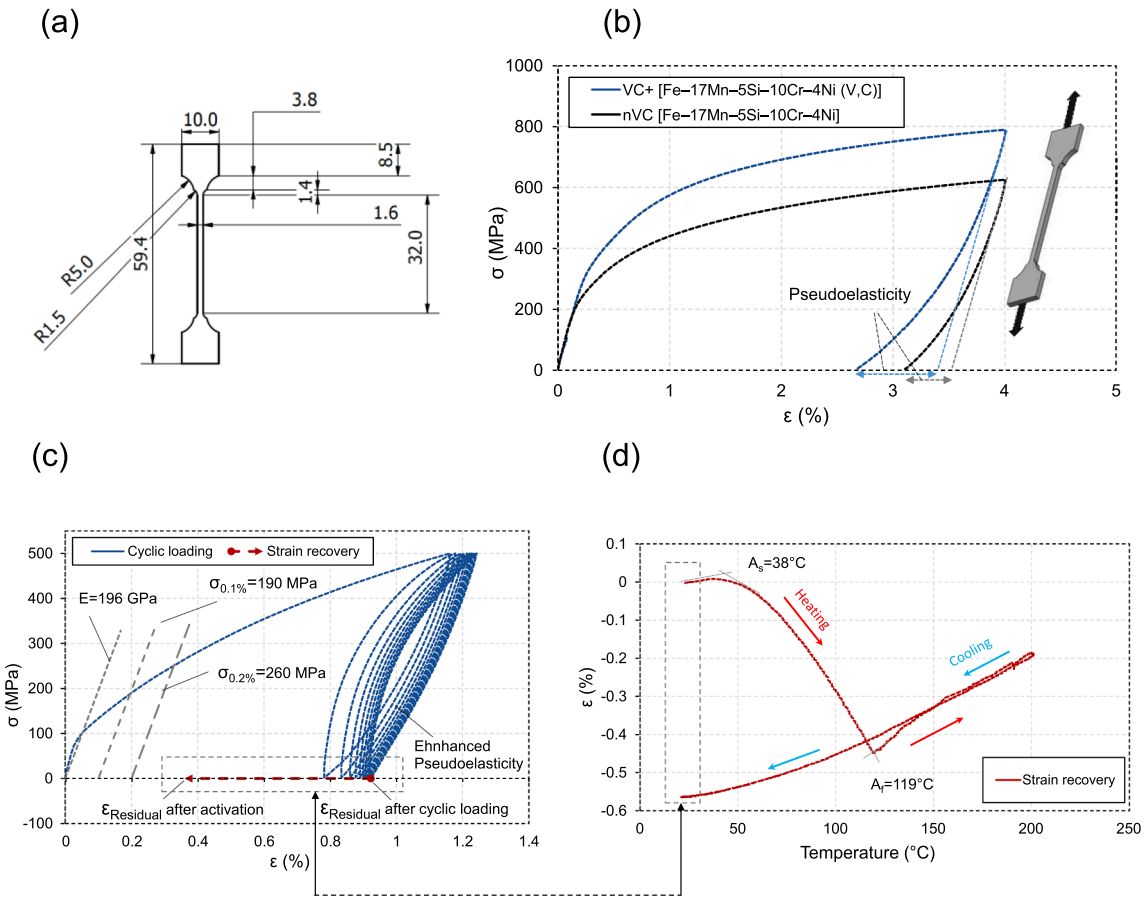

Fig. 4. Material behavior of tensile dog-bone specimens. a) Drawing of the dog-bone-shaped specimen used in the measurement of PE and SME of VC + and nCV materials. b) Load-unload response of the dog-bone-shaped specimen until 4%. c) Cyclic loading–unloading behavior (under constant stress level of 500 MPa) of a VC + Fe-SMA tensile dog-bone specimens, b) Recovery strain as a function of the temperature after cyclic loading–unloading.

Table 2
Chemical compositions of the Fe-based SMA powders.

Powder	Fe (wt. %)	Mn (wt. %)	Cr (wt. %)	Si (wt. %)	Ni (wt. %)	V (wt. %)	C (wt. %)
nVC	Bal.	17.0	9.9	4.6	4.6	–	–
VC+	Bal.	17.7	10.1	4.5	4.3	0.7	0.2

Table 3
Selected build parameters for the 3D printing of Fe-SMAs using L-PBF.

	Laser power (W)	Scanning speed (mm/s)	Layer thickness (mm)	Hatch spacing (mm)	Scanning strategy
nVC	175	300	0.03	0.1	0°-90°, bi-directional
VC+	175	225	0.03	0.1	0°-90°, bi-directional

pseudo-elasticity, was investigated. Consequently, aging at 750 °C for 6 h was selected for the present investigation, as the pseudoelastic behavior of the alloy for these conditions is significantly enhanced.

2.2. Mechanical characterization

2.2.1. Tests on additively-manufactured Fe-SMA material

Both nVC and VC + dog-bone-shape specimens were subjected to loading up to 4% strain and unloading to 5 N force tensile test and also cyclic loading and unloading tensile tests were carried out on the dog-bone-shaped specimens utilizing a universal tensile testing machine (Z020, Zwick/Roell). In cyclic test, dog-bone-shaped tensile specimen was repeatedly loaded to a defined stress (500 MPa) and subsequently was unloaded to a constant force of 10 N, at a constant displacement rate of 0.5 mm/min. The 500 MPa stress level is correspondent to an average stress in critical location of the BIA Fe-SMA during loading as shown in Fig. 2c. Activation processes were performed on dog-bone-shaped tensile specimen to measure the recovery strain of the printed material. After subjecting the tensile specimen to a cyclic loading–unloading followed by a subsequent heating process, a partial recovery of the residual strain due to the SME of the Fe-based SMA, namely, recovery strain, was achieved. It is important to note that recovery strain can be achieved when the tensile specimen moves freely back to its primary shape. The universal Zwick machine with a climate-controlled chamber was used to measure the recovery strain of the pre-strained tensile specimen. The tensile specimens were subjected to a constant preloading of approximately 5 N during the heating and cooling cycles. Then, the temperature was increased from 23 °C to 200 °C at a rate of 2 °C/min. The specimens were then held at 200 °C for 30 min, followed by cooling to 23 °C at a rate of 2 °C/min. The strains in the tensile specimen were continuously recorded using a clip-on extensometer (with a gauge length of 20 mm) during the heating/cooling cycle. The ultimate strain recorded at the end of the test was considered as the recovery strain.

2.2.2. Tests on BIA Fe-SMAs

Quasi-static compression tests on the BIA Fe-SMAs were also conducted using the same universal testing machine. The default load cell of the machine with 20kN capacity was replaced with a 2 kN load cell to

enhance the measurement accuracy. Cyclic displacement-controlled loading and unloading tests were performed to investigate the recoverability and energy absorption/dissipation capabilities of BIA Fe-SMAs. The samples were cyclically loaded to the densification point and unloaded to a holding force of 2 N for six sequences. Deification occurs when the internal elements i.e. curved and straight beams come into self-contact and therefore, the axial stiffness approaches the bulk stiffness. The force–displacement (F–δ) response of the samples was measured, where δ is the induced compressive displacement and F is the corresponding reaction force. For each cycle, the shape-recovery ratio was calculated as follows: $R_r = \frac{\delta_r}{\delta_m}$, which is the ratio of the recovered displacement after unloading (δ_r) to the maximum induced compressive deformation (δ_m). To characterize the ability of further deformation recovery upon heating associated with the SME of the alloy, additional experiments were performed in a climate chamber attached to the testing machine. The samples were then heated to 200 °C with a heating rate of 2 °C/min. The temperature was constantly maintained for 30 min at the maximum temperature (200 °C) to ensure homogenous heating of the sample. Finally, the chamber was cooled down to the room temperature at the rate of 2 °C/min. The final height of the samples at the end of the heating and cooling cycles were measured and compared with the residual deformations recorded during the cyclic test.

3. Results and discussion

3.1. Microstructural and mechanical analysis of additively-manufactured Fe-SMAs

According to previous investigations, the high heat input introduced during the process caused a certain loss in Mn due to evaporation [44,45,49]. For similar applied processing parameters, the amount of Mn (13.5 wt%) reduces of more than 4 wt% compared to the initial Mn content of the powder [49]. The alloy's chemical composition plays an important role in the deformation behavior of SMAs, affecting the phase transformation temperatures, the austenite stability and the material's stacking fault energy (SFE) [50–54]. In Fe-Mn-Si [55], a minimum SFE is observed for Mn contents between 10 and 15 wt% at RT. Therefore, the evaporation of Mn might promote the martensitic de-formation by decreasing the SFE of the material, and thus, favoring the formation of stacking faults and hcp martensite.

Fig. 3 shows the microstructure of the two printed Fe-SMAs after the heat treatment. Precipitates form in both the samples after heat treatment. According to previous studies [44,48], the coarse precipitates at the grain boundaries of the nVC samples are rich in Cr and Si and form during heat treatment between 700 °C and 900 °C. The addition of C to the VC + alloy causes the precipitation of fine carbides (V-carbides) at the grain boundaries and within the grains. Carbides are rather fine and high in number, as depicted in Fig. 3.

3.2. Material behaviour of additively-manufactured Fe-SMA

For the evaluation of thermomechanical behavior of the printed Fe-SMA, single tensile test up to 4% strain were applied on both printed Fe-SMAs after the heat treatment and the stress–strain curves are presented in Fig. 4b. The mechanical properties such as pseudoelasticity, Young's modulus, and yield stress of the samples can be derived from stress-strain curves as shown in Fig. 4. The results indicated that VC + sample has a greater strength at 4% strain than nVC sample and also shows a strong work-hardening behavior due to presence of carbides in microstructure. Furthermore, VC + sample displays higher pseudoelasticity and absorb energy than nVC sample. The formation of uniform distribution V-carbide precipitates after heat treatment in VC + sample led to the formation of stacking faults and ε-martensite in the microstructure and interaction of precipitates with the martensite plate tips provided spring back stress for revers transformation (martensite to austenite) resulting in improved the pseudoelasticity and also increased work-hardening in the aged sample [39,56]. Since cyclic loading–unloading tensile test and activation process were applied on the aged VC + dog-bone-shaped specimen.

Fig. 4c shows the cyclic loading–unloading (under constant stress level of 500 MPa) behavior. During loading, the nonlinear deformation behavior after elastic deformation is due to martensitic transformation, followed by both plastic and martensitic transformation. For this alloy, a 0.1% yield stress ($\sigma_{0.1\%} = 190$ MPa) is more appropriate to estimate the stress onset for martensite transformation than a 0.2% yield stress ($\sigma_{0.2\%} = 260$ MPa). In the first cycle after unloading, the absolute recovery strain is 0.34%. Therefore, there is a considerable residual strain in this step (0.78%). However, the residual strain is significantly reduced in the next cycles. In the first cycle, the microstructure of the tensile specimen is austenitic and the stress-induced martensite forms during loading. A part of the martensite transforms back to austenite during unloading (i.e., PE). A part of the remaining martensite in the structure can turn into austenite during activation process and as a result, a part of residual strain recovers (SME).

Fig. 4d shows the recovery strain as a function of temperature after cyclic loading–unloading. Generally, the strain curves can be divided into four stages during one cycle of heating and cooling. During heating from the room temperature, the strain increases with the increasing temperature because of the thermal expansion (first stage). With a further increase in the temperature, the martensite to austenite transformation begins above austenitic start temperature (A_s) due to the SME and results in a decrease in the strain up to austenitic finish temperature (A_f, second stage). Above A_f, the transformation of the martensite to the austenite has been completed, and the increasing strain as a result of the further thermal expansion of the austenite can be measured (third stage). After cooling, the strain decreases linearly owing to the thermal contraction of the tensile specimen (fourth stage). Therefore, the A_s and A_f temperatures can be obtained from the strain–temperature curves, as shown in Fig. 4d. Furthermore, Fig. 4d demonstrates that the recovery strain due to the SME is about 0.58% which indicates that 75% of residual strain could be recovered after the activation. The same thermomechanical behavior was observed for the BIA Fe-SMA samples under cyclic compression test, which will be discussed in the next section.

3.3. Structural behaviour of the BIA Fe-SMAs

Cyclic loading–unloading tests were performed on both of the nVC and VC + BIA Fe-SMAs samples. Fig. 5a and b show the force–displacement (F–δ) responses of the samples under displacement-controlled compression tests. Videos 1 and 2, which are attached as supplementary files to this article, demonstrate the loading and unloading process of the nVC and VC + samples, respectively.

Samples were initially loaded to 8 mm for the first cycle at a rate of 2 mm/min, and after 20 s of holding at the maximum displacement, they were unloaded at the same rate up to a reaction force of 2 N. The first cycle in both VC + and nVC samples contained four pronounced peaks in the reaction forces. Each of the four peaks is associated with the snap-through of a curved beam row in the sample, followed by a negative stiffness region. The first cycles of the samples similarly exhibited the highest force threshold and energy absorption compared with the subsequent cycles. However, the lowest shape-recovery ratio, R_r, was also associated with the first cycle with 79 and 87% for nVC and VC+, respectively, as shown in Fig. 5c. The shape-recovery of the samples after unloading is due to the elastic strain recovery, PE, and monostability of the curved beams. The residual deformation is associated with the formation of martensite from the parent austenite phase, as well as irreversible plastic deformation. This phenomenon occurs in strain-demanding locations that can be found in the simulation results (Fig. 2c and 2f) close to the curved-beam joints.

The BIA Fe-SMA samples were cyclically loaded for an additional five

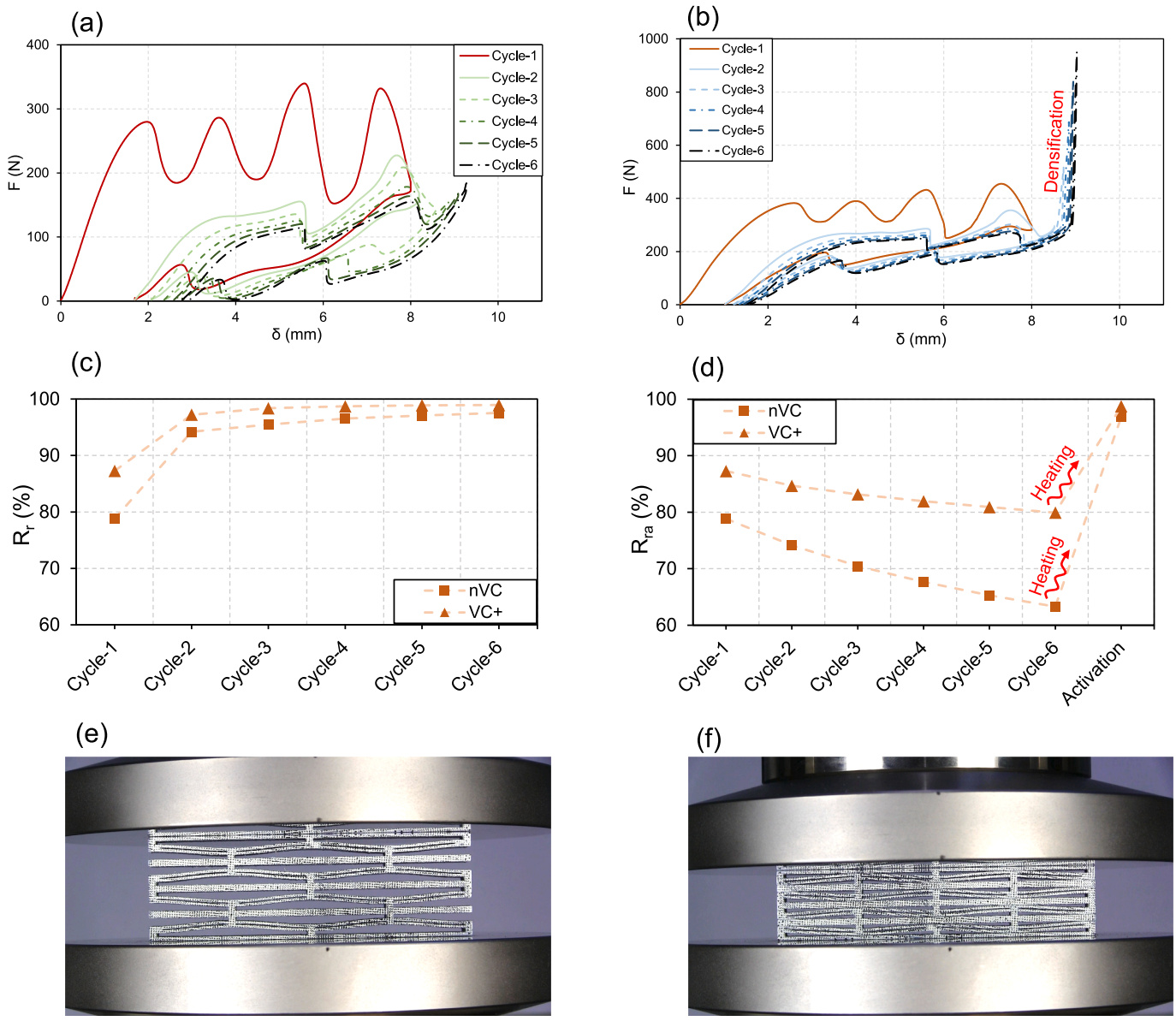

Fig. 5. Cyclic displacement-controlled compression tests on the nVC and VC + BIA Fe-SMA samples. a) Force–displacement (F-δ) response of the nVC sample under cyclic compression tests. The first cycle holds a higher force threshold yet exhibits significantly higher residual displacement. b) Force-displacement response of the VC + sample under cyclic compression tests. Densification occurred for the succeeding cycles after the first loading cycle due to excessive loading. The same pattern as the nVC sample is found in the F–δ response of the VC + sample. c) Comparison of the shape-recovery ratio (R_r) for each loading cycle. d) Accumulative shape-recovery ratio (R_{ra}) after each loading cycle is plotted up to each loading cycle. Ultimately,R_{ra} was counterbalanced upon activation (through heating) of samples due to SME. e) The BIA Fe-SMA sample before loading. f) BIA Fe-SMA at the maximum compressive displacement. Videos 1 and 2 (see the attached as supplementary files to this article) show the time-history of the loading and unloading process of the nVC and VC + samples, respectively.

cycles after the first cycle. Owing to the considerable permanent deformation in the first cycle, the strain demand on the curved beams decreased. Therefore, the BIA Fe-SMA samples exhibited a lower force threshold than the first cycle. In both VC + and nVC samples, almost identical responses for the subsequent cycles after the first cycle (Fig. 5a and b) was observed. In this stage, the response of the samples was stable and represented a flag-shaped response with negligible residual deformation, which is, R_r of 94–99% as shown in Fig. 5c. The nVC and VC + samples were compressed to 6.5 mm and 7.5 mm for the last five cycles, respectively. In the VC + sample, excessive displacement was applied and the sample entered the densification region, as shown in Fig. 5b. During densification, the sample exhibited a bulk-like response, in which a sudden increase in the reaction force occurred as a result of minimal displacement. It should be noted that in contrast to conventional crushable lattices, the BIA Fe-SMA samples could reconfigure the initial shape without being damaged after densification.

Fig. 5d shows the accumulative shape-recovery ratio (R_{ra}) at each stage, which after the sixth cycle, reaches 80% and 63% for the VC + and nVC samples, respectively. R_r after unloading in all cycles was greater for the VC + sample than for the nVC sample. The main reason for this phenomenon can be attributed to the enhanced PE and strength of the VC + alloy promoted by the presence of precipitates.

Ultimately, both samples were heated up to 200 °C at a heating rate of 2 °C/min and maintained at the maximum temperature for 30 min. This led to R_{ra} of 96.8 and 98.7 for nVC and VC + BIA Fe-SMA samples, respectively. This shape recovery is ascribed to SME, which is activated upon heating. The negligible residual deformation during cyclic loading is attributed to plastic deformation phenomena, which is, irreversible slip and plastic deformation. This proves the possibility of fabricating architected materials with significant energy absorption/dissipation

capacities in a reusable manner.

3.4. Energy absorption capability

By further processing the quasi-static cyclic experiments on the VC + and nVC BIA Fe-SMAs samples, their energy absorption was calculated and plotted against the nominal strain, which is presented in Fig. 6a and b. The nominal strain (ε_n) is defined as δ/H, which is the ratio of the compressive displacement δ to the initial height of the samples at the beginning of the loading cycle (H = 26.6 for both BIA Fe SMA samples). The energy absorption is expressed as follows:

$$W_a = \int_0^{\delta_m} F(\delta)d\delta \tag{2}$$

where W_a is the absorbed energy, δ_m is the maximum compressive displacement, and F is the reaction force. From Fig. 6a and b, it can be observed that both VC + and nVC samples exhibit similar patterns, where a significantly higher energy is absorbed during the first cycle. However, the VC + sample absorbs more energy for each cycle than the nVC sample. This is because of the higher strength of the base alloy, which is associated with the formation of precipitates in the VC alloy used for the VC + sample. This observation can be attributed to the fact that the precipitates increase the strength of the material by hindering the movement of dislocations (i.e., precipitation hardening) [57].

In Fig. 6a and b, each curve can be divided into loading and unloading paths. The loading path extended to δ_m where it had the maximum absorbed energy. The unloading path begins from δ_m and represents the amount of energy the lattice releases during unloading and ends at the energy dissipation state. Similarly, in both structures, the responses of the subsequent cycles after the first cycle are almost

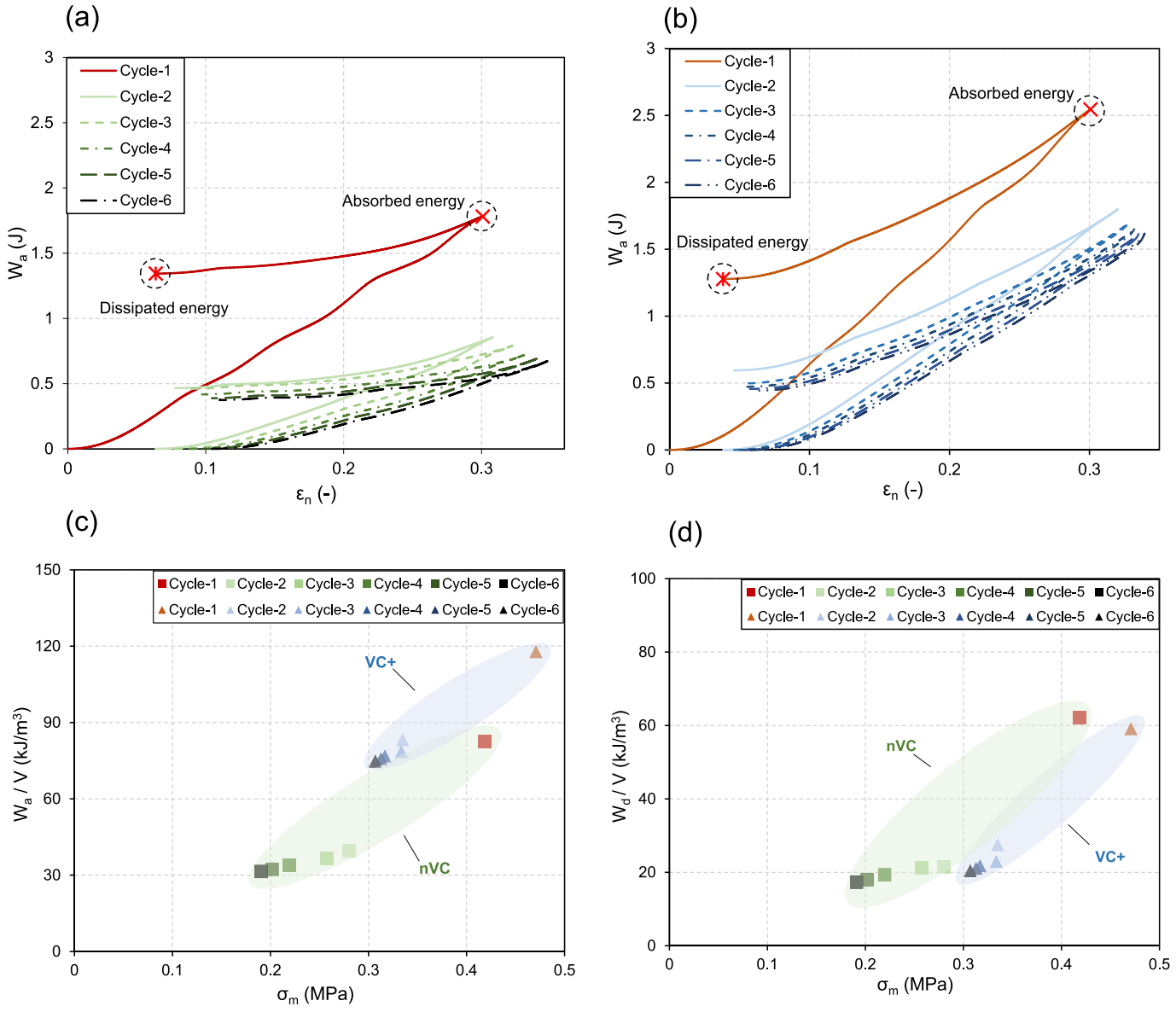

Fig. 6. Energy absorption/dissipation in the BIA Fe-SMA samples. a) Energy absorption of the nVC sample during loading and unloading paths. The total absorbed energy is highlighted at the end of loading–maximum induced strain. The unloading path corresponds to the amount of energy that the samples released. The difference between the absorbed and released energies is the dissipated energy highlighted in the first cycles. b) Energy absorption of the VC + sample during loading and unloading paths. Similar to the nVC sample, VC + exhibits the highest energy absorption/dissipation in the first loading cycle. c) The Ashby diagram of the SEA (W_a/V) against the compressive strength (σ_m) of the nVC and VC + samples. SEA is more significant in the VC + sample at each corresponding cycle. d) The Ashby map diagram of the SED (W_d/V) against the compressive strength σ_m of the nVC and VC + samples. Despite the significantly higher SEA in VC + sample, nVC exhibits a similar performance regarding energy dissipation.

identical, indicating a stable response of the structures in terms of energy absorption.

Specific energy absorption/dissipation (SEA/SED) for both structures is expressed as follows:

$$SEA/SED = \frac{W_{a/d}}{V} \quad (3)$$

where SEA/SED is the absorbed/dissipated energy per unit volume, $W_{a/d}$ is the absorbed/dissipated energy, and V is the volume occupied by each sample. Fig. 6c and 6d show the Ashby plot, where the SEA and SED are plotted against the compressive strength (σ_m) for the structures, respectively. The compressive strength was defined as the maximum force during the plateau divided by the loading plane area ($\sigma_m = F/b \bullet l$).

Similar to the F-δ_m response, the SEA and SED for both structures can be classified into two groups: the first and the following cycles. The first cycle in both structures was associated with the highest SEA/SED, and concurrently the highest compressive strength. Moreover, the VC + sample exhibits a higher SEA compared to the nVC sample, which is attributed to the higher strength of the VC + Fe-SMA because of the formation of precipitates. Remarkably, the energy dissipation in the nVC sample was slightly greater than that in the VC + sample in the first cycle, and was nearly constant in the following cycles. This implies that despite the lower energy absorption and compressive strength, the nVC sample exhibited a nearly equal energy dissipation with respect to the VC + sample. However, this significant energy dissipation in the nVC sample is to the cost of a greater residual deformation in comparison with VC + sample.

Fig. 7 shows the Ashby map of the absorbed energy per unit volume against the compressive strength for the present work (nVC, VC +) BIAMs and those in the literature. The BIA Fe-SMAs exhibit a pronounced specific energy absorption and compressive strength compared to similar BIAMs. A higher compressive strength in BIA Fe-SMAs implies that it is able to hold a higher dead-load before it reaches the force threshold and is considered as a load-carrying element and an energy absorber. Furthermore, the higher SEA and strength in the first cycle compared to the following cycles in BIA Fe-SMAs make them suitable for applications where a major initial impact is followed by a sequence of minor loading cycles. Moreover, BIA Fe-SMAs, as shown in this study, are able to recover their initial shape after experiencing cyclic loading, which may make them stand out among existing impact and vibration isolation solutions. Fig. 8 illustrates a few potential real-world scenarios where integration of 4D printed BIA Fe-SMAs leads to energy absorption/dissipation in a reusable manner. Potential applications in landing legs of reusable rocket, integration of BIA Fe-SMAs in bumper beams, vibration isolation for resilient buildings and construction as well as in wind turbine nacelles are a few examples for applications of 4D printed BIA Fe-SMAs.

In general, a relatively low modulus of elasticity and glass transition temperature limit the performance of polymeric architected materials in comparison with BIA Fe-SMAs. Thus, BIA Fe-SMAs can potentially be used for applications such as passive impact and vibration isolation, as they exhibit advanced serviceability and ultimate performance. If designed properly, BIA Fe-SMAs are able to undergo large deformations without being damaged. Moreover, owing to the SME, the BIA Fe-SMA is able to recover its original shape to be utilized and reused several times. The results in this study demonstrated that by 4D printing of BIA Fe-SMAs, the material-inherent functional behavior can be combined with the functionalities of the architected structure to achieve a superior multi-functionality behavior.

4. Conclusion

This study introduces a novel class of BIAM made of iron-based Fe-Mn-Si-Cr-Ni shape memory alloys that can exhibit a significant amount of energy dissipation as well as shape recovery. The geometry of two Fe-SMAs were architected to a mono-stable negative-stiffness configuration to achieve an enhanced recentring/recoverability behavior. It was shown that by 4D printing of BIA Fe-SMAs, the inherent functional behavior of the shape memory alloys can be added up to the functionalities of the engineered structure to obtain a greater multi-functionality response. The following conclusions were drawn from this study:

- Combining the mono-stable architecture with a smart base material (in this study, Fe-SMA) can result in advanced functionalities in terms of recoverability and energy absorption and dissipation.

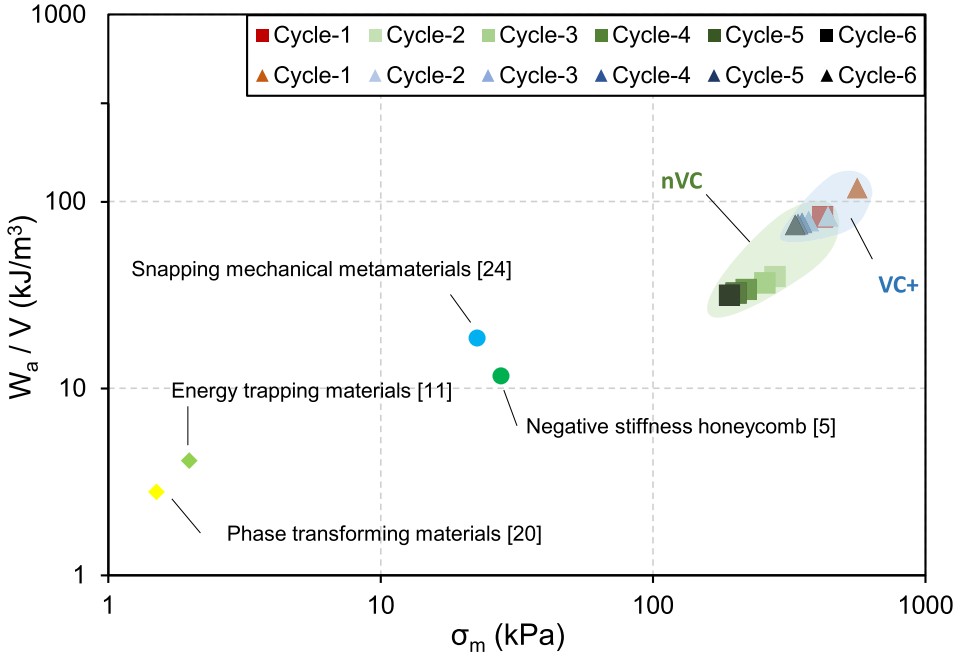

Fig. 7. Ashby plot of energy absorption per unit volume versus the compressive strength for previously reported BIAMs and the proposed BIA Fe-SMAs in this study.

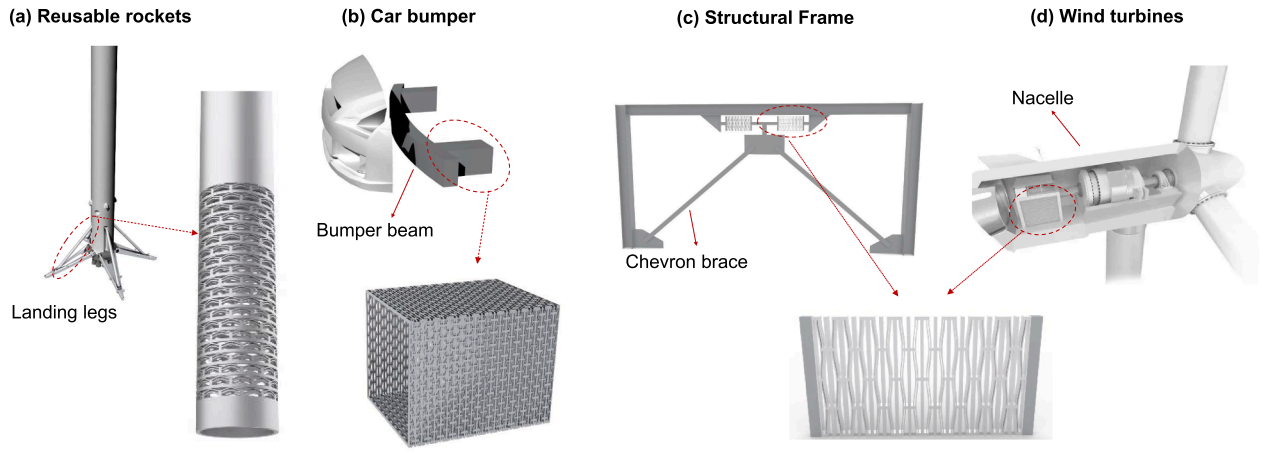

Fig. 8. Illustration of a few real-world scenarios where integration of BIA Fe-SMAs can be explored for passive impact and vibration isolation. a) Potential application in landing legs of reusable rocket, b) integration of BIA Fe-SMAs in bumper beams, c) vibration isolation for resilient buildings and construction, d) passive dampers for wind turbine nacelles.

- Compared to polymeric BIAMs, BIA Fe-SMAs exhibit a greater force threshold, recoverability, energy absorption, and dissipation owing to the enhanced SME and PE of the base material.
- Quasi-static cyclic compression tests indicated that both samples (nVC and VC +) similarly exhibited the highest energy absorption/dissipation in the first loading cycle; nevertheless, recoverability increased in the subsequent cycles to 94 and 99% for the nVC and VC + samples, respectively.
- The VC + sample exhibited higher SEA, PE, and compressive strength, which can be associated to the presence of precipitates in the alloy. However, in the nVC samples, almost similar SED to that of the VC + samples was observed.
- Activation of the cyclically-loaded samples led to accumulated shape-recovery ratios (R_{ra}) of 96.8 and 98.7% for the nVC and VC + samples, respectively. The samples nearly recovered their full original shapes after the accumulation of residual deformations during cyclic loading.

In conclusion, this study highlights the potential of 4D printed BIA Fe-SMAs to achieve superior multi-functionality behavior by combining the material's inherent functional behavior with the functionalities of the engineered structure, rendering them ideal for applications like passive impact and vibration isolation.

Declaration of Competing Interest

The authors declare that they have no known competing financial interests or personal relationships that could have appeared to influence the work reported in this paper.

Data availability

Data will be made available on request.

Acknowledgements

The authors thank voestalpine BÖHLER Edelstahl GmbH & Co KG for providing the powders for the LPBF experiments. The support of re-fer AG in providing Fe-SMAs for the test specimens is gratefully acknowledged. Furthermore, the authors would like to thank the laboratory staff of the Structural Engineering Research Laboratory at Empa for their support in performing the experiments.

Appendix A. Supplementary data

Supplementary data to this article can be found online at https://doi.org/10.1016/j.matdes.2023.112216.

References

[1] F. Craveiro, J.P. Duarte, H. Bartolo, P.J. Bartolo, Additive manufacturing as an enabling technology for digital construction: a perspective on Construction 4.0, Automation in Construction 103 (2019) 251–267.
[2] Y. Zhang, D. Restrepo, M. Velay-Lizancos, N.D. Mankame, P.D. Zavattieri, Energy dissipation in functionally two-dimensional phase transforming cellular materials, Sci. Rep. 9 (1) (2019) 1–11.
[3] S. Ford, M. Despeisse, Additive manufacturing and sustainability: an exploratory study of the advantages and challenges, J. Clean. Prod. 137 (2016) 1573–1587.
[4] S. Chen, X. Tan, J. Hu, S. Zhu, B. Wang, L. Wang, Y. Jin, L. Wu, A novel gradient negative stiffness honeycomb for recoverable energy absorption, Engineering, Composites Part B, 2021, p. 215.
[5] Correa, D.M., Design and evaluation of negative stiffness honeycombs for recoverable shock isolation. 2015.
[6] S. Chen, B. Wang, S. Zhu, X. Tan, J. Hu, X.u. Lian, L. Wang, L. Wu, A novel composite negative stiffness structure for recoverable trapping energy, Compos. A Appl. Sci. Manuf. 129 (2020) 105697.
[7] D.A. Debeau, C.C. Seepersad, M.R. Haberman, Impact behavior of negative stiffness honeycomb materials, J. Mater. Res. 33 (3) (2018) 290–299.
[8] X. Tan, B. Wang, S. Chen, S. Zhu, Y. Sun, A novel cylindrical negative stiffness structure for shock isolation, Compos. Struct. 214 (2019) 397–405.
[9] X. Tan, B. Wang, S. Zhu, S. Chen, K. Yao, P. Xu, L. Wu, Y. Sun, Novel multidirectional negative stiffness mechanical metamaterials, Smart Mater. Struct. 29 (1) (2020) 015037.
[10] Wang, B., X. Tan, S. Zhu, S. Chen, K. Yao, P. Xu, L. Wang, H. Wu, and Y. Sun, *Cushion performance of cylindrical negative stiffness structures: Analysis and optimization.* Composite Structures, 2019. **227**.
[11] S. Shan, S.H. Kang, J.R. Raney, P. Wang, L. Fang, F. Candido, J.A. Lewis, K. Bertoldi, Multistable architected materials for trapping elastic strain energy, Adv. Mater. 27 (29) (2015) 4296–4301.
[12] S. Kamrava, D. Mousanezhad, H. Ebrahimi, R. Ghosh, A. Vaziri, Origami-based cellular metamaterial with auxetic, bistable, and self-locking properties, Sci. Rep. 7 (2017) 46046.
[13] O. Rehme, C. Emmelmann, Selective laser melting of honeycombs with negative Poisson's ratio. 4 (2009) 128–134.
[14] X. Yu, J. Zhou, H. Liang, Z. Jiang, L. Wu, Mechanical metamaterials associated with stiffness, rigidity and compressibility: a brief review, Prog. Mater Sci. 94 (2018) 114–173.
[15] Z. Xiong, M. Li, S. Hao, Y. Liu, L. Cui, H. Yang, C. Cui, D. Jiang, Y. Yang, H. Lei, Y. Zhang, Y. Ren, X. Zhang, J.u. Li, 3D-printing damage-tolerant architected metallic materials with shape recoverability via special deformation design of constituent material, ACS Appl. Mater. Interfaces 13 (33) (2021) 39915–39924.
[16] C. Huang, Y. Zheng, T. Chen, E. Ghafoori, L. Gardner, Fatigue crack growth behaviour of wire arc additively manufactured steels, Int. J. Fatigue 173 (2023), 107705.
[17] E. Ghafoori, H. Dahaghin, C. Diao, N. Pichler, L. Li, M. Mohri, J. Ding, S. Ganguly, S. Williams, Fatigue strengthening of damaged steel members using wire arc additive manufacturing, Eng. Struct. 284 (2023), 115911.
[18] I.O. Felice, J. Shen, A.F.C. Barragan, I.A.B. Moura, B. Li, B. Wang, H. Khodaverdi, M. Mohri, N. Schell, E. Ghafoori, T.G. Santos, J.P. Oliveira, Wire and Arc Additive

Manufacturing of Fe-based shape memory alloys: microstructure, mechanical and functional behavior, Mater. Des. 231 (2023), 112004.
[19] Y. Li, S. Yu, Y. Chen, R. Yu, Y. Shi, Wire and arc additive manufacturing of aluminum alloy lattice structure, J. Manuf. Process. 50 (2020) 510–519.
[20] D. Restrepo, N.D. Mankame, P.D. Zavattieri, Phase transforming cellular materials, Extreme Mech. Lett. 4 (2015) 52–60.
[21] Y. Zhang, M. Velay-Lizancos, D. Restrepo, N.D. Mankame, P.D. Zavattieri, Architected material analogs for shape memory alloys, Matter 4 (6) (2021) 1990–2012.
[22] M. Corsi, S. Bagassi, M.C. Moruzzi, F. Weigand, Additively manufactured negative stiffness structures for shock absorber applications, Mech. Adv. Mater. Struct. 29 (7) (2022) 999–1010.
[23] T. Frenzel, C. Findeisen, M. Kadic, P. Gumbsch, M. Wegener, Tailored Buckling Microlattices as Reusable Light-Weight Shock Absorbers, Adv. Mater. 28 (28) (2016) 5865–5870.
[24] A. Rafsanjani, A. Akbarzadeh, D. Pasini, Snapping mechanical metamaterials under tension, Adv. Mater. 27 (39) (2015) 5931–5935.
[25] A. Brinkmeyer, M. Santer, A. Pirrera, P.M. Weaver, Pseudo-bistable self-actuated domes for morphing applications, Int. J. Solids Struct. 49 (9) (2012) 1077–1087.
[26] H. Yang, L. Ma, Multi-stable mechanical metamaterials by elastic buckling instability, J. Mater. Sci. 54 (4) (2018) 3509–3526.
[27] C.S. Ha, R.S. Lakes, M.E.J.M. Plesha, Design, fabrication, and analysis of lattice exhibiting energy absorption via snap-through behavior. 141 (2018) 426–437.
[28] J. Qiu, J.H. Lang, A.H. Slocum, A curved-beam bistable mechanism, J. Microelectromech. Syst. 13 (2) (2004) 137–146.
[29] Tan, X., S. Zhu, B. Wang, K. Yao, S. Chen, P. Xu, L. Wang, and Y. Sun, Mechanical response of negative stiffness truncated-conical shell systems: experiment, numerical simulation and empirical model. Composites Part B: Engineering, 2020. **188**.
[30] H. Yang, L. Ma, 1D and 2D snapping mechanical metamaterials with cylindrical topology, Int. J. Solids Struct. 204–205 (2020) 220–232.
[31] N. Hu, R. Burgueño, Buckling-induced smart applications: recent advances and trends, Smart Mater. Struct. 24 (6) (2015) 063001.
[32] M. Alturki, R. Burgueño, Response characterization of multistable shallow domes with cosine-curved profile, Thin-Walled Struct. 140 (2019) 74–84.
[33] M. Alturki, R. Burgueño, Multistable Cosine-Curved Dome System for Elastic Energy Dissipation, J. Appl. Mech. 86 (9) (2019).
[34] S. Cortes, J. Allison, C. Morris, M.R. Haberman, C.C. Seepersad, D. Kovar, Design, Manufacture, and Quasi-Static Testing of Metallic Negative Stiffness Structures within a Polymer Matrix, Exp. Mech. 57 (8) (2017) 1183–1191.
[35] X. Tan, S. Chen, S. Zhu, B. Wang, P. Xu, K. Yao, Y. Sun, Reusable metamaterial via inelastic instability for energy absorption, Int. J. Mech. Sci. 155 (2019) 509–517.
[36] S. Kajiwara, Characteristic features of shape memory effect and related transformation behavior in Fe-based alloys, Mater. Sci. Eng. A 273 (1999) 67–88.
[37] A. Cladera, B. Weber, C. Leinenbach, C. Czaderski, M. Shahverdi, M. Motavalli, Iron-based shape memory alloys for civil engineering structures: An overview, Constr. Build. Mater. 63 (2014) 281–293.
[38] L. Janke, C. Czaderski, M. Motavalli, J. Ruth, Applications of shape memory alloys in civil engineering structures—overview, limits and new ideas, Mater. Struct. 38 (5) (2005) 578–592.
[39] M. Mohri, I. Ferretto, C. Leinenbach, D. Kim, D.G. Lignos, E. Ghafoori, Effect of thermomechanical treatment and microstructure on pseudo-elastic behavior of Fe–Mn–Si–Cr–Ni-(V, C) shape memory alloy, Mater. Sci. Eng. A 855 (2022) 143917.
[40] H. Khodaverdi, M. Mohri, E. Ghafoori, A.S. Ghorabaei, M. Nili-Ahmadabadi, Enhanced pseudoelasticity of an Fe–Mn–Si-based shape memory alloy by applying microstructural engineering through recrystallization and precipitation, J. Mater. Res. Technol. (2022).
[41] C. Leinenbach, H. Kramer, C. Bernhard, D. Eifler, Thermo-Mechanical Properties of an Fe-Mn-Si-Cr-Ni-VC Shape Memory Alloy with Low Transformation Temperature, Adv. Eng. Mater. 14 (1–2) (2012) 62–67.
[42] Qiu, J., *An electrothermally-actuated bistable MEMS relay for power applications*. 2003, Massachusetts Institute of Technology.
[43] J. Hua, H. Lei, C.-F. Gao, X. Guo, D. Fang, Parameters analysis and optimization of a typical multistable mechanical metamaterial, Extreme Mech. Lett. 35 (2020), 100640.
[44] I. Ferretto, D. Kim, N.M. Della Ventura, M. Shahverdi, W. Lee, C. Leinenbach, Laser powder bed fusion of a Fe–Mn–Si shape memory alloy, Addit. Manuf. 46 (2021), 102071.
[45] I. Ferretto, D. Kim, M. Mohri, E. Ghafoori, W.J. Lee, C. Leinenbach, Shape recovery performance of a (V, C)-containing Fe-Mn-Si-Ni-Cr shape memory alloy fabricated by laser powder bed fusion, J. Mater. Res. Technol. 20 (2022) 3969–3984.
[46] W.J. Lee, B. Weber, G. Feltrin, C. Czaderski, M. Motavalli, C. Leinenbach, Phase transformation behavior under uniaxial deformation of an Fe–Mn–Si–Cr–Ni–VC shape memory alloy, Mater. Sci. Eng. A 581 (2013) 1–7.
[47] D. Kim, I. Ferretto, C. Leinenbach, W. Lee, 3D and 4D Printing of Complex Structures of Fe Mn Si-Based Shape Memory Alloy Using Laser Powder Bed Fusion, Advanced Materials Interfaces 9 (13) (2022) 2200171.
[48] M. Mohri, I. Ferretto, H. Khodaverdi, C. Leinenbach, E. Ghafoori, Influence of thermomechanical treatment on the shape memory effect and pseudoelasticity behavior of conventional and additive manufactured Fe–Mn–Si–Cr–Ni-(V, C) shape memory alloys, J. Mater. Res. Technol. 24 (2023) 5922–5933.
[49] I. Ferretto, A. Borzì, D. Kim, N.M.D. Ventura, E. Hosseini, W.J. Lee, C. Leinenbach, Control of microstructure and shape memory properties of a Fe-Mn-Si-based shape memory alloy during laser powder bed fusion, Additive Manufacturing Letters 3 (2022), 100091.
[50] N. Stanford, D.P. Dunne, B.J. Monaghan, Austenite stability in Fe–Mn–Si-based shape memory alloys, J. Alloy. Compd. 430 (1) (2007) 107–115.
[51] J.C. Li, M. Zhao, Q. Jiang, Alloy design of FeMnSiCrNi shape-memory alloys related to stacking-fault energy, Metall. Mater. Trans. A 31 (3) (2000) 581–584.
[52] G. Meric de Bellefon, J.C. van Duysen, K. Sridharan, Composition-dependence of stacking fault energy in austenitic stainless steels through linear regression with random intercepts, J. Nucl. Mater. 492 (2017) 227–230.
[53] M. Wendler, J. Mola, L. Krüger, A. Weiß, Experimental Quantification of the Austenite-S tabilizing Effect of Mn in Cr M n N i As-C ast Stainless Steels, Steel Res. Int. 85 (5) (2014) 803–810.
[54] Q. Dai, X. Cheng, Y. Zhao, X. Luo, Z. Yuan, Design of martensite transformation temperature by calculation for austenitic steels, Mater Charact 52 (4–5) (2004) 349–354.
[55] O.A. Zambrano, Stacking Fault Energy Maps of Fe–Mn–Al–C–Si Steels: Effect of Temperature, Grain Size, and Variations in Compositions, J. Eng. Mater. Technol. 138 (4) (2016).
[56] H. Khodaverdi, M. Mohri, A.S. Ghorabaei, E. Ghafoori, M. Nili-Ahmadabadi, Effect of low-temperature precipitates on microstructure and pseudoelasticity of an Fe–Mn–Si-based shape memory alloy, Mater Charact 195 (2023), 112486.
[57] Y. Yang, A. Arabi-Hashemi, C. Leinenbach, M. Shahverdi, Influence of thermal treatment conditions on recovery stress formation in an FeMnSi-SMA, Mater. Sci. Eng. A 802 (2021), 140694.